World Electric Vehicle Journal

Article

Efficiency Analysis of Hybrid Extreme Regenerative with Supercapacitor Battery and Harvesting Vibration Absorber System for Electric Vehicles Driven by Permanent Magnet Synchronous Motor 30 kW

Pataphiphat Techalimsakul and Pakornkiat Sawetmethikul *

Program in Electronics and Automation Systems Engineering, Faculty of Technical Education, Rajamangala University of Technology Thanyaburi, Pathum Thani 12110, Thailand; pataphiphat_t@rmutt.ac.th
* Correspondence: pkkt@rmutt.ac.th; Tel.: +668-5491-4241

Abstract: This research presents an approach to the hybrid energy harvesting paradigm (HEHP) based on suspended energy harvest. It uses a harvesting vibration absorber (HVA) with an SC/NMC-lithium battery hybrid energy storage paradigm (SCB-HESP) equipped regenerative braking system (SCB-HESP-RBS) for electric vehicles 2 tons in gross weight (MEVs) driven by a 30 kW permanent magnet synchronous motor (PMSM). During regenerative braking, the ANN mechanism controls the RBS to adjust the switching waveform of the three-phase power inverter, and the braking energy transfers to the energy storage device. Additionally, a supercapacitor (SC) equipped with HVA can absorb energy from vehicle vibrations and convert it into electrical energy. The energy-harvesting efficiency of MEV based on SCB-HESP-RBS using HVA suspended energy harvesting enhances the efficiency maximum to 50.58% and 15.36% in comparison to MEV with only-HVA and SCB-HESP-RBS, respectively. Further, the MEV with SCB-HESP-RBS using HVA has a driving distance of up to 247.34 km (22.5 cycles) when compared with SCB-HESP-RBS (214.40 km, 19.5 cycles) and only-HVA (164.25 km, 15 cycles).

Keywords: electric vehicles; harvesting vibration absorber; hybrid energy harvesting paradigm; energy storage

check for updates

Citation: Techalimsakul, P.; Sawetmethikul, P. Efficiency Analysis of Hybrid Extreme Regenerative with Supercapacitor Battery and Harvesting Vibration Absorber System for Electric Vehicles Driven by Permanent Magnet Synchronous Motor 30 kW. *World Electr. Veh. J.* **2024**, *15*, 214. https://doi.org/10.3390/wevj15050214

Academic Editor: Joeri Van Mierlo

Received: 20 March 2024
Revised: 20 April 2024
Accepted: 7 May 2024
Published: 12 May 2024

1. Introduction

At present, direct greenhouse gas emissions from internal combustion engines result in increased air pollution. In particular, land transportation is the primary source of air pollution in urban areas. Faced with deteriorating air quality, many countries around the world, including Europe, the United States, Japan, and China, have embraced electric vehicles (EV) as a solution to combat carbon emissions from fossil fuels [1,2]. The replacement of internal combustion vehicles with electric vehicles has begun to play a role in many countries around the world. Because there are zero emissions from the exhaust pipe, this reduces the amount of CO_2 emissions associated with driving. This contributes to improved air quality in urban areas, especially if electric vehicles apply new technology to create comfort and are safe to drive [1–5]. Electricity is typically less expensive than gasoline, and electric vehicles have fewer moving parts, leading to reduced maintenance costs. In some regions, governments and organizations offer incentives, such as carbon credits or offsets, to encourage the adoption of electric vehicles. Most electric vehicle batteries still use electrochemical batteries for their main energy storage systems. Electrochemical batteries still have many limitations, such as short life cycles, low energy density, high cost, and limited driving range, which affect regenerative braking performance later [6,7]. Energy storage technology is a turning point in the contemporary automotive industry, with the potential to enhance vehicle energy efficiency and the fuel economy. In the scope of electric vehicle technologies, the focus primarily centers on harvesting energy from regenerative braking and vehicular suspension-induced vibrations [8,9]. Moreover, achieving efficient regenerative braking necessitates the inclusion of a sizable energy storage system comprising multiple battery packs.

To address these limitations, a hybrid energy storage paradigm was employed, incorporating multiple SC and batteries, to enhance vehicle acceleration and extend the longevity of the battery. Various energy management strategies have been suggested in the literature to optimize power distribution in a hybrid energy storage paradigm [10]. Most of the previous research has proposed fuel cell systems with SC and batteries. Comparable energy management approaches can also be applied to SC/battery hybrid configurations. Approaches grounded in heuristics or empirical knowledge can be readily put into practice through the utilization of rule-based control algorithms or by employing fuzzy logic methodologies. In addition, straightforward filter-based or frequency-based power distribution strategies have been incorporated as demonstrated in [11]. In the context of a traditional electric vehicle, a considerable quantity of energy is expended during urban driving cycles due to braking [11].

To enhance the efficiency of EV, the RBS was devised [12]. This system makes use of the electric motor, which applies negative torque to convert kinetic energy into electrical energy, thereby replenishing the energy storage devices. Effectively harnessing the dissipation of kinetic energy during braking is achieved through meticulous control of the vehicle's onboard power electronics for comprehensive energy management. Consequently, regenerative braking proves to be a highly effective technology for enhancing the overall efficiency of electric vehicles. Numerous efforts to meet the control performance requirements for regenerative braking have been documented in the literature, such as rule-based strategies [13], PID control strategies [11–14], and ANN approaches [15]. In situations where regenerative braking is active, the DC-link voltage experiences a rise, prompting the RBS program, with the assistance of the ANN controller, to redirect the energy from braking towards storage in the SC. The SC has SCB-HESP-powered scenario density and high battery energy density, but there are still limitations in using high-power electronic interfaces as a bidirectional dc/dc chopper is required to connect the battery to the SC, which leads to higher costs [9–14] and high-power electronic systems. The interface causes energy dissipation, and regenerative braking performance decreases later.

In practice, a vibration absorber or damper is a mechanical device designed to absorb and stimulate damp vibrations by converting the kinetic energy of the impact into another form of energy. Then that efficiency is distributed to the control condition, explanation, and strength that comes from the system, which causes a beneficial effect on driving for a longer time [16,17]. Typically, vehicles traverse uneven roads, and in such scenarios, a harvesting vibration absorber can transform the linear vibration of the suspension into electricity through an electromagnetic circuit. Regenerative suspension, which uses electromagnetic harvesting, stands out as one of the most widely used harvesting technologies in automotive energy harvesting, as mentioned in the literatures. The electromagnetic-equipped harvester has gained prominence and is becoming increasingly attractive due to its high-energy conversion efficiency, simple design, rapid response, strong controllability, and ability to recover energy [18–21].

Several energy harvesting-related suspension systems have been proposed and optimized accordingly. This ensures better performance when there are differences in usage. In addition, regenerative braking is already presented and is also applied to hybrid and commercial electric vehicles. However, both suspension systems for energy harvesting and regenerative braking are still under development. Both energy harvesting methods have limitations when the total weight increases and there is a need for additional space, system loss, loss of efficiency, and cost.

This research proposes a combination of the HEHP based on the SCB-HESP-RBS and using energy suspended by HVA for an MEV driven by PMSM 30 kW. In regenerative braking conditions, the DC-link voltage is stimulated. Installation of the ANN program in the RBS results in the optimal switching pattern of the three-phase inverter. Transfer braking energy to store in SC this harvest can increase the MEV driving range and extend battery life [22–25].

2. The SCB-HESP Regenerative Scenario

The regenerative braking scenario under SC activates an increase in the DC-link voltage, causing the power diode to become forward-conducting, thus establishing a boost circuit within the three-phase inverter. The high side of the switch of the half-bridge is closed and the bottom of the switch is pulse width-modulated. The regenerated braking energy is then transferred and stored in the SC module. A buck-boost dc/dc chopper is used to help transfer braking energy to SC as shown in Figure 1, (a) SC-activated regenerative braking scenario by HVA, and (b) SC-activated regenerative braking by RBS.

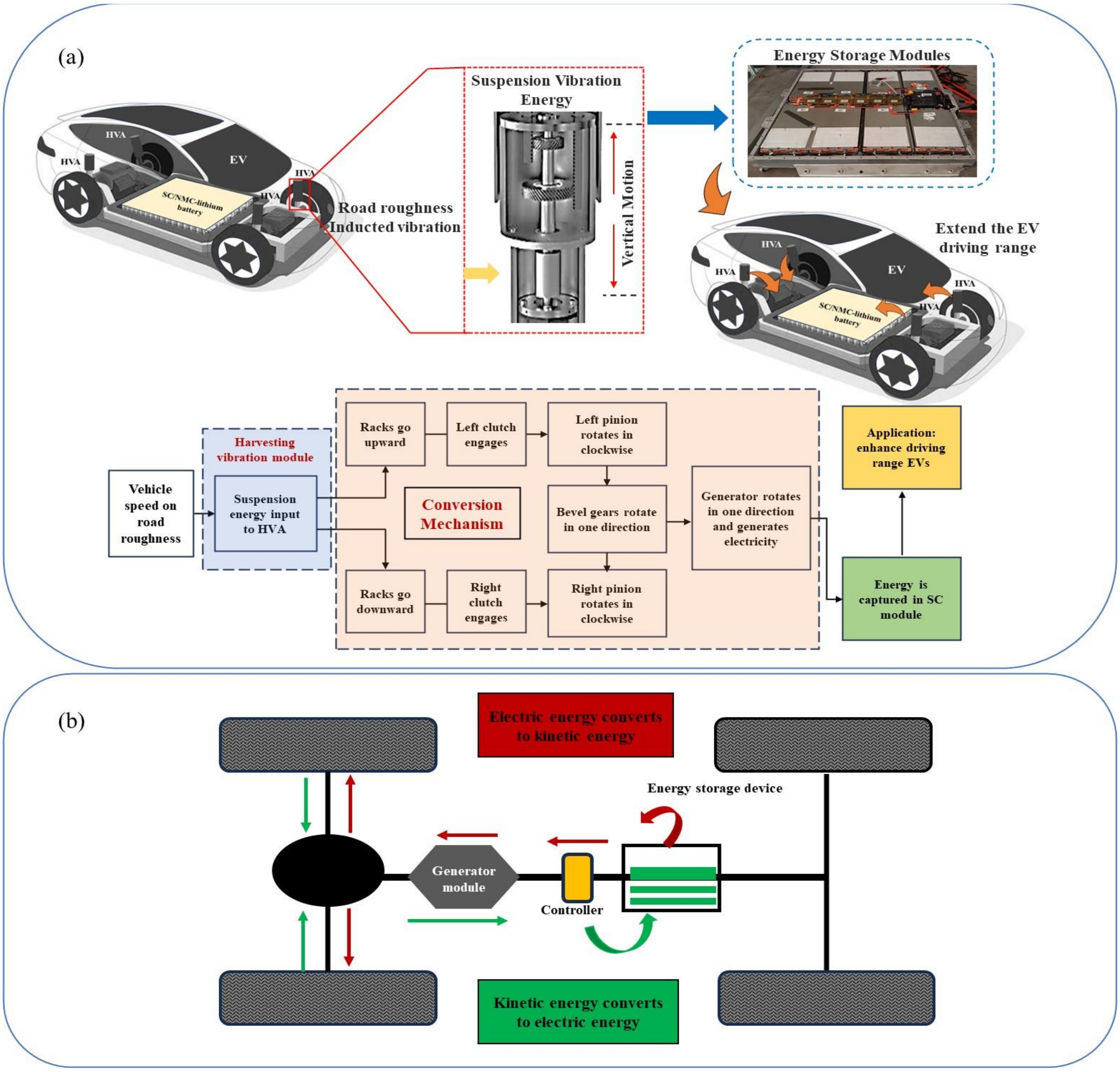

Figure 1. The system of the hybrid energy-harvesting paradigm. (**a**) SC-activated regenerative braking by HVA. (**b**) SC-activated regenerative braking by RBS.

3. The Harvesting Vibration Absorber Design

This research combined the outstanding efficiency and other relevant factors of SC and batteries: SC is highly efficient in terms of charging/discharging rates and cycle life. Integration with traditional batteries leads to high energy density, but may have limitations in terms of charging/discharging rates [6]. Specific information about SC and batteries is shown in Table 1. Further, the application of SC-equipped HVA reduces unwanted vibrations, which can lead to a loss of energy. HVA is designed to absorb and dampen the shock impulses and vibrations generated by uneven road surfaces, bumps, and other disturbances to improve energy efficiency in electric vehicles [9]. Figure 1a illustrates the proposed scheme for the HVA equipped with an SC. It comprises three key components: the suspension harvesting system, a conversion mechanism, and energy storage modules.

Table 1. The parameter characteristics of SC and battery.

Parameter	Battery	Supercapacitor
Cell type	NMC	EDLC
Cell voltage	~3.6–4.2 V	~2.1–3.3 V
Service life	~5–10 years	~10+ years
Specific energy	100–200 Wh/kg	5 Wh/kg
Series/Parallel	1P96S	-
Cell amount (pcs)	96	140
System Capacity	196 Ah	3000 F
System Energy (kWh)	60	-
System Voltage (V)	355.2	380
System voltage ranger (V)	269.8 to 412.8	-
Continuous charging current of maximum (A)	169	200
Continuous discharging current of maximum (A)	169	200
Weight (kg)	400	-
Temperature charging temp	0 to 50 °C	−40 to 65 °C
Temperature discharging temp	−20 to 60 °C	−40 to 65 °C
Battery assembly SOC	30% ± 3%	-
Time of charge/discharge	10–90 min	5–15 s

3.1. The Suspension Harvesting System

Figure 2 illustrates the placement of the harvesting vibration absorber, which is installed between the vehicle frame and the chassis. Both the outer and inner cylinders of the vibration absorber are attached to the vehicle's frame. While driving on rough roads or accelerating and decelerating, the vibrations of the suspension vibrations generate linear movement between the two cylinders. Indeed, road roughness and vehicle speed are the primary factors contributing to suspension vibrations [26]. In Figure 3, the simulation example of suspension velocity between the unsprung mass and the sprung mass of the proposed vibration absorber at a speed of 45 km/h is shown. This simulation was conducted using CarSim with BMW X and the HB106-Class pavement scenario. The maximum instantaneous speed recorded was 65 km/h. Suspension speed simulations were conducted over a range of vehicle speeds, from 35 km/h to 70 km/h [6]. While the vehicle traveled at 45 km/h, the sprung and unsprung mechanisms worked in tandem to ensure a balanced and controlled interaction with the road surface. Suspension systems play an important role in managing forces and movement between sprung and unsprung masses. This affects the overall performance, vehicle control, and driving comfort [9].

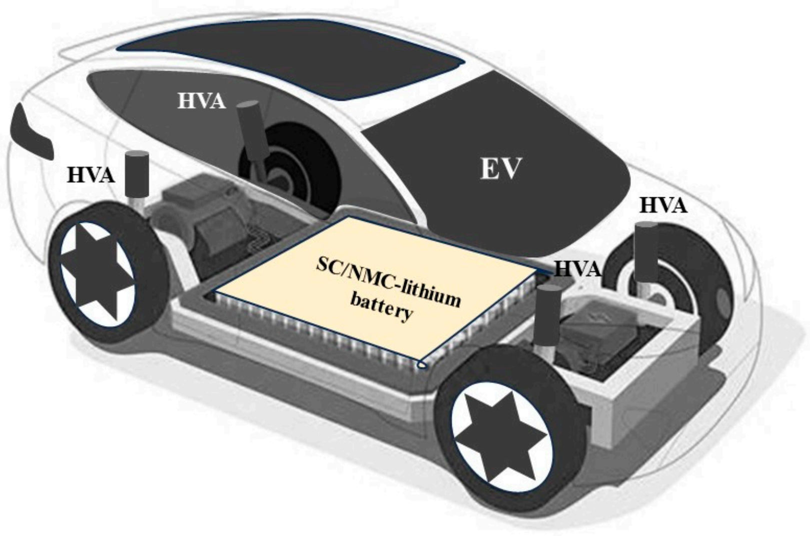

Figure 2. Position of the proposed harvesting vibration absorber.

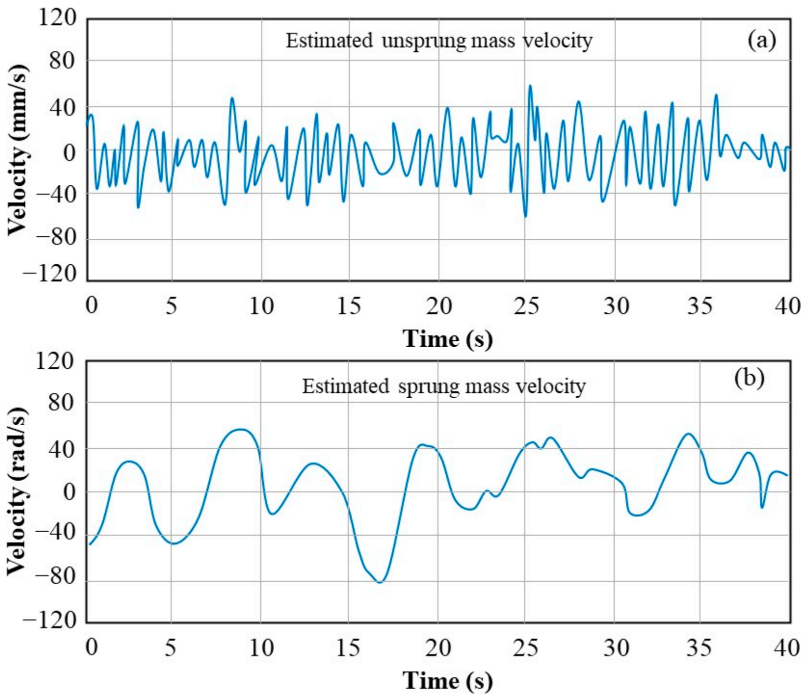

Figure 3. The CarSim simulated suspension mass velocity at 45 km/h: (**a**) estimated unsprung; (**b**) estimated sprung [6].

3.2. The Conversion Mechanism

This conversion mechanism is a file that converts bidirectionally between the inner and outer cylinders. Linear movement (up–down) becomes a unidirectional rotation to drive the generator shaft. Figure 4a shows the prototype and 3D scenario of HVA consisting of two cylinders, as well as bevel gears overrunning clutch, rack pinion, shaft, and interior gear. Figure 4b shows a shaft with two gears assembled without being stationary in one direction. An overrunning clutch (CSK-PP type) is installed at the shaft and attached to the gear.

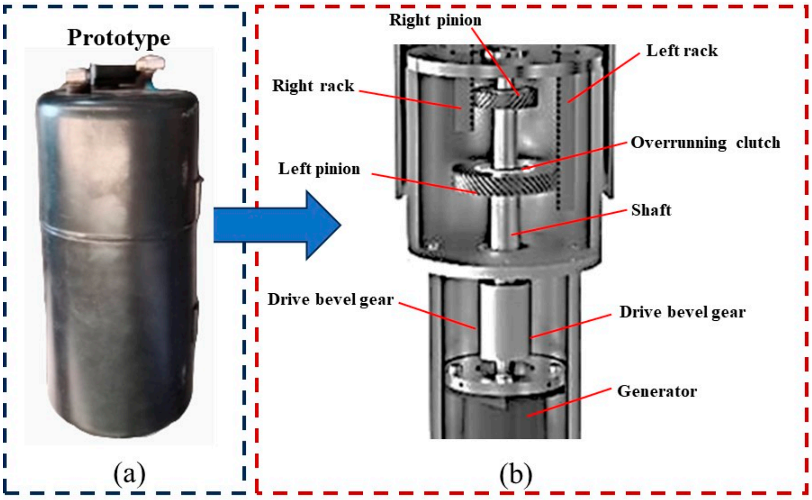

Figure 4. The prototype and 3D scenario of the HVA: (**a**) outer and (**b**) inner structure.

When the vehicle vibrates, there is an alternating pattern of movement between the inner and outer cylinders. The linear movement causes movement up and down the shelf. Then, the shelf sends vertical movement in the left-right wing direction. In rack and pinion assembly, the two pinions rotate in opposite directions [6]. For the couple type, the overrun clutch alternately engages and disengages the shaft, which results in a single direction. The rotational movement of the output shaft independent of shelf movement is shown in Figure 5.

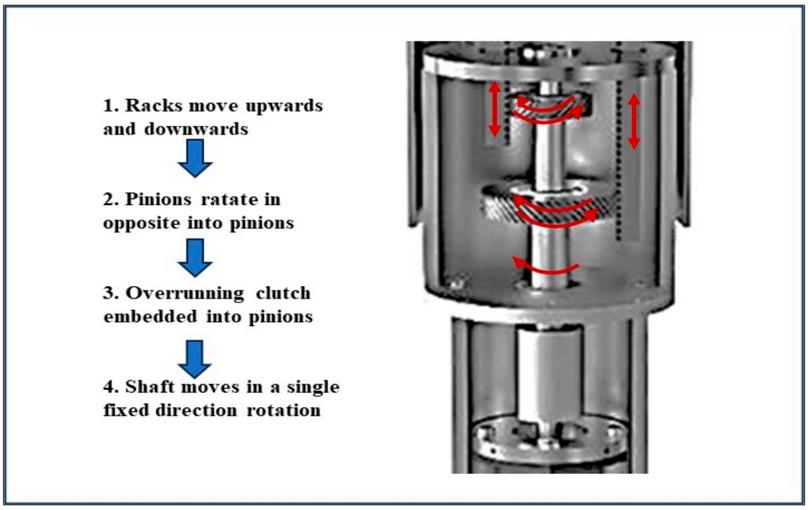

Figure 5. The conversion mechanism with bidirectional linear motion into a unidirectional rotation.

3.3. The Energy Storage Module

The frequency and amplitude of suspension vibration are contingent on both road roughness and vehicle speed. Swift changes in suspension vibration frequency and amplitude lead to fluctuations in the generator's rotational speed, resulting in an unstable regenerative current. To address this issue, a PMSM motor can serve as a three-phase alternating current (AC) generator. However, a three-phase current is not well-suited for recharging batteries or powering electrical loads. To convert a three-phase alternating current into a pulsed current, a voltage regulator employing the LM311N8 as a stabilivolt is utilized in an energy storage module (Figure 6a). Moreover, the rapid fluctuations in the frequency and amplitude of vibrations within suspension systems require the incorporation of SC for efficient storage of the pulse-like current. Figure 6b illustrates the rectifier circuit [6].

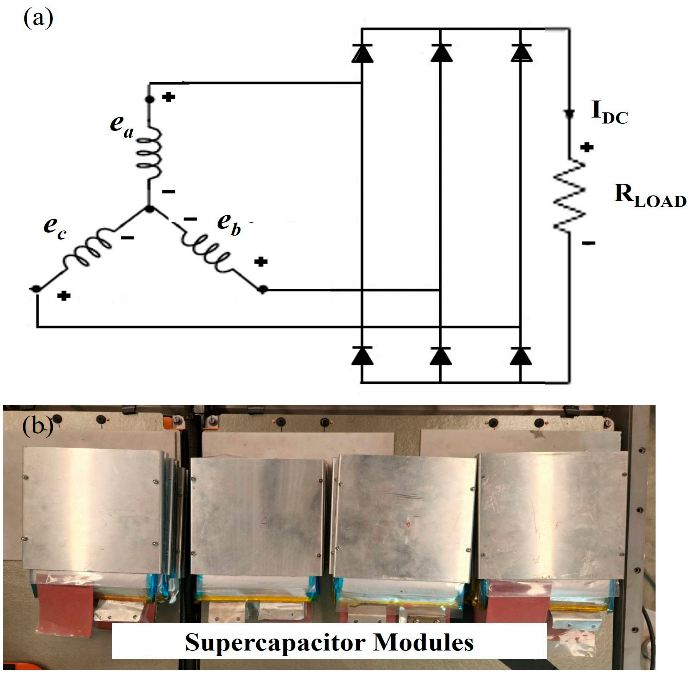

Figure 6. The rectifier circuit converts the three-phase alternating current into a constant, pulse-like current: (**a**) diagram; (**b**) the supercapacitor circuit.

4. System Power Analysis

This research proposes a type of system power analysis which investigates the effects of HVA model parameters, such as the damping force and impulse force, on the efficiency of output power. The damping force (F_{damp}) of HVA can be expressed as [27]:

$$\begin{gathered} F_{damp} = F_e = m_{eq}\ddot{o} + L_c = m_{cylinder} + 2m_{rack} + \\ \frac{\frac{I_g}{I^2} + I_{pg} + I_b + I_s + 2I_p}{r^2} \times \ddot{x} \\ \frac{1.5 \times k_e^2}{E_{gen}E_{plangear}E_{bevel}E_{rack}p^2r^2(R_{external} + R_{internal})} \times \dot{x} \end{gathered} \tag{1}$$

where F_{damp} is the force with damping; F_e is the force of excitation; o is the speed of excitation; and E_{gen}, $E_{plangear}$, E_{bevel}, and E_{rack} are the efficiencies of the generator, planetary gearbox, bevel gear, and rack-pinion, respectively. $m_{cylinder}$ and m_{rack} are the masses of the outer cylinder and the rack, respectively. On the other hand, I_{pg}, I_s, I_p, I_b, and I_g refer to the inertia of the planetary gearbox, shaft, pinion, bevel gear, and generator. K_e signifies the rotary damping coefficient, while $R_{internal}$ is the internal resistor within each phase of the generator charging circuit, and $R_{external}$ is the external resistor. The variables r, p, and L_c correspond to the pinion radius, planetary gear ratio, and linear damping coefficient, respectively [6].

The mechanical efficiency (E_m) of the HVA can be mathematically expressed as

$$E_m = E_{gen}E_{plangear}E_{bevel}E_{rack} \tag{2}$$

Substituting (2) into (1) yields:

$$E_mP_{input} = P_{electrical} \tag{3}$$

where $P_{electrical}$ is the electrical power, which consists of both the fragment charge harvesting $(P_{harvesting})$ and the portion lost to the internal resistance $(P_{in,lost})$ of the generator. The calculation for the fragment lost to internal resistance can be expressed as

$$\boldsymbol{P_{electrical} = P_{harvesting} + P_{in,lost}} \tag{4}$$

Therefore, the electrical efficiency of the HVA can be calculated using the following formula:

$$\boldsymbol{E_e = \frac{P_{harvesting}}{P_{harvesting} + P_{in,lost}}} \tag{5}$$

When considering mechanical performance and electrical performance. Therefore, the total efficiency of a HVA is:

$$\beta = \beta_m \cdot \beta_e \tag{6}$$

where β_e is electrical efficiency, β_m is mechanical efficiency, and the total efficiency of the HVA is β.

The linear damping coefficient can be determined through the following formula [27]:

$$\boldsymbol{L_c = \frac{\Delta W}{\pi \omega A^2}} \tag{7}$$

where ΔW is the mechanical work input of the harvesting vibration absorber, and ω and A are the frequency and amplitude of the sinusoidal vibration, respectively.

Further, the total efficiency (β) of HVA can also be calculated by:

$$\beta = \boldsymbol{\frac{P_{output}}{P_{input}}} \tag{8}$$

where P_{output} stands for the average power output of HVA per cycle or electrical power and P_{input} stands for the average input power or mechanical power of the HVA per cycle. Referring to Equation (6), the mechanical efficiency of HVA can be found as follows:

$$\beta m = \boldsymbol{\frac{\beta}{\beta_e}} \tag{9}$$

Referring to Equation (5), the electrical efficiency of HVA is 0.89. Therefore, the input power (mechanical power) of HVA per cycle can be calculated as:

$$P_{input} = \boldsymbol{\frac{\Delta W}{T}} \tag{10}$$

where ΔW is the mechanical work data of HVA and T is the period of sinusoidal stimulation.

5. Design of Bench Test Experimental

This research used PMSM motors to use permanent magnets to provide field excitation. These motors generate higher torque and have more efficiency than BLDC motors. The PMSM 30 kW is designed to be more compact and lightweight. This can result in savings in terms of vehicle weight, which can improve the overall efficiency of the vehicle and reduce energy consumption. Table 1 is the simulation parameter of HESP in a different value between the battery and supercapacitor. Additionally, Table 2 shows specific information about the parameters of the PMSM motor. Figure 7 shows the design and experimental test of the harvesting vibration absorption system. Figure 8 proposes a tachograph model of the driving cycle of an NEDC vehicle. This driving cycle is a frequent urban driving scenario. In addition, Table 3 shows the NEDC drive cycle parameters of electric vehicles.

Table 2. Experimental test of permanent magnet synchronous motor parameters.

Symbols	Parameters	Value
P_{mt}	Power of maximum transfer	60,000 Watt
A_{rt}	Average rated torque	96 N·m
A_{rp}	Average rated power	30,000 Watt
M_{torque}	Maximum of torque	240 N·m
$I_{current}$	Maximum of current	275 Amp
A_{rc}	Average rated current	100 Amp
A_{ts}	Average tated speed	3000 rpm
F	Frequency	150 Hertz
M_{speed}	Maximum of speed	6000 rpm
T_c	Torque constant	0.87 N·m/A
B_{EMF}	Back-EMF	165 Volts
P_{phase}	Phase–phase resistance	0.01 Ω
P_{pairs}	Pole pairs	3

Figure 7. Design experiment of hybrid energy-harvesting paradigm: (**a**) test bench experiment in electric vehicle; (**b**) equipment design in electric vehicle.

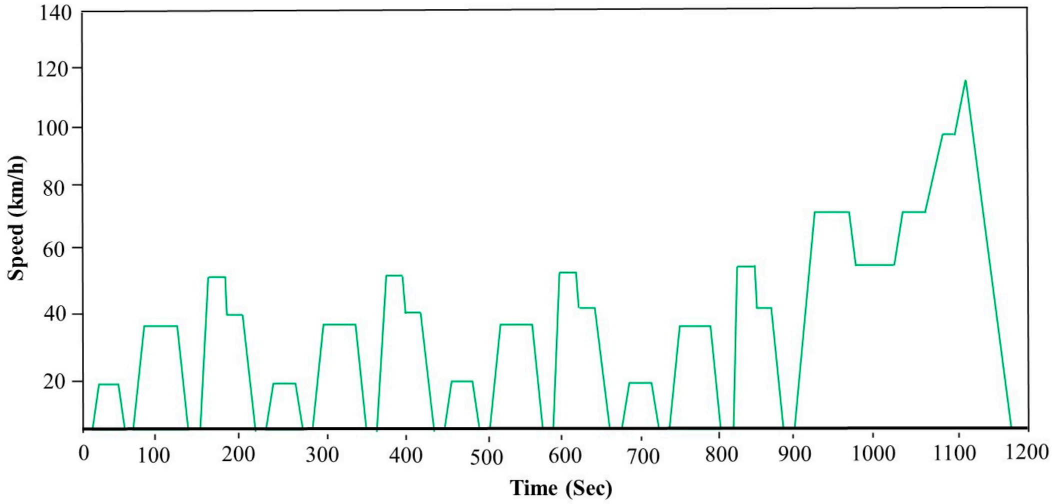

Figure 8. Pattern of the driving cycle of an NEDC vehicle.

Table 3. The NEDC drive cycle parameters of electric vehicles.

Parameter	Value	Unit
Cycle name	NEDC	-
Driving distance	10.95	km
Total time	906.10	s
Accelerating time (%)	21.78	%
Decelerating time (%)	15.19	%
Braking time (%)	19.68	%
Stop duration (%)	24.05	%
Speed of average	33.26	km/h
Speed of maximum	111.22	km/h
Average positive acceleration	0.59	m/s^2
Average negative acceleration	−0.48	m/s^2

6. Experimental Results and Discussion

The HVA bench-test experiments were conducted under sinusoidal vibration conditions with varying frequencies of 2.5, 3, 3.5, and 4 Hz and amplitudes of 3.5, 7, and 10.5 mm to observe the force–displacement loops. Due to dimensional constraints, the prototype HVA had a maximum amplitude of 10.5 mm. The experimental platform for the HVA prototype involved the use of an HS-5051-AF3 electronic shock absorber testing system and power, and Figure 9 shows data analysis of power, current, and voltage CAN communication using a YOKOGAWA DL350 oscilloscope. Furthermore, Table 4 provides the experimental findings, including the kinetic energy before braking and the energy stored after braking, based on the speed just before braking, which averages 12.51 m/s over a braking duration of 10 s. The energy recovered after braking averages 3838.81 joules, while the kinetic energy before braking averages 28,367.76 joules. The recovered energy of the system harvesting vibrations at different speeds before braking shows in Figure 10.

Figure 11 presents both simulation and experimental data illustrating the relationship between speed and the time required for braking within a range of 10.38 s, starting from an initial speed of 48.13 km/h. This evaluation was conducted to assess the supercapacitor pressure before and after braking. The simulation results indicate that, during the preceding period and after 10.38 s of braking at an average speed of 48.13 km/h before braking, the supercapacitor voltage increased to 6.44 V.

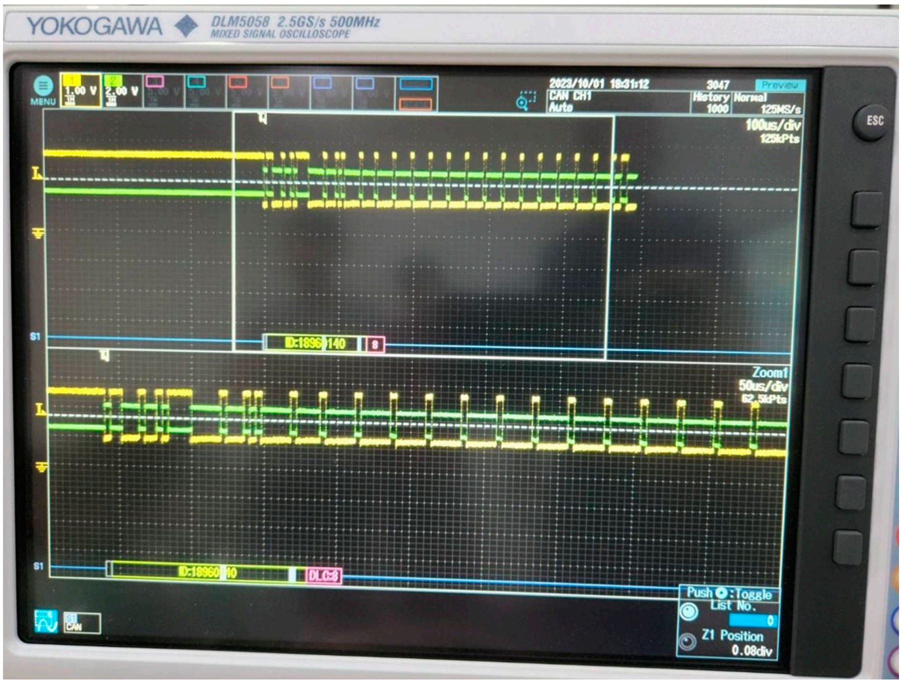

Figure 9. Experimental power and data analysis using YOKOGAWA DL350, including power, current, and voltage CAN communication.

Table 4. Experimental and simulation specifications.

Set	Speed before Braking (m/s)	Final Speed after Braking (m/s)	Total Kinetic Energy before Braking (J)	Duration of Braking (s)	Energy Recovered (J)
1	10.40	10.26	28,350.21	10.32	3130.81
2	10.63	10.54	29,714.69	10.57	2918.37
3	10.27	10.23	27,157.05	10.14	4194.13
4	10.39	10.19	28,428.82	10.22	4031.68
5	10.78	10.48	28,188.02	10.55	4919.05

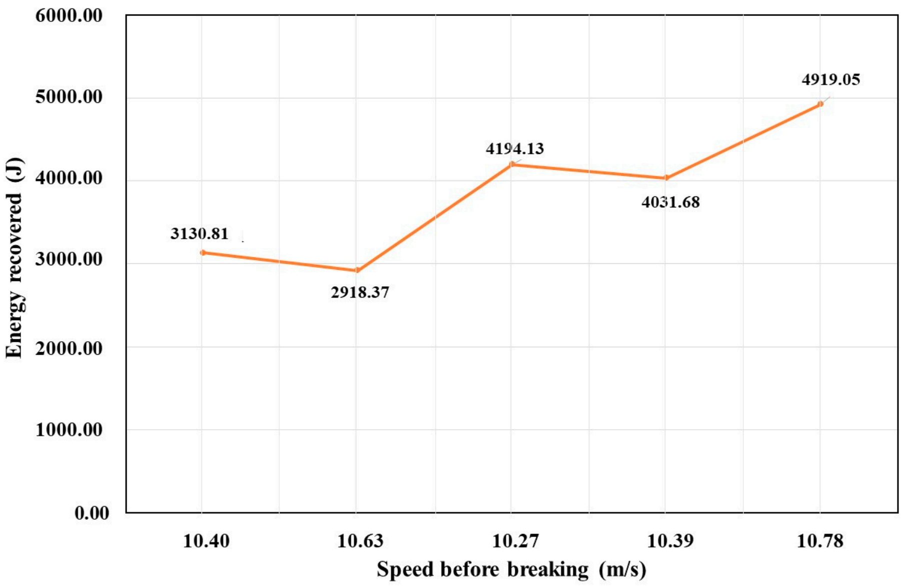

Figure 10. The recovered energy curve of the harvesting vibration absorption system at different speeds before braking.

The efficiency of the proposed method can be assessed by comparing the state of charge (SOC) of the hybrid energy storage device throughout the driving cycle of MEV. Figure 12a,b gives a comparison between simulations and experiments for the charge statuses of both the SC and the NMC-lithium battery under two conditions: The system recovers braking using the SC, starting with an initial charge status of 88.4% for SC and 87.2% for the NMC-lithium battery. When the system recovers braking using the battery, the SOC values of the SC and NMC-lithium batteries start at 98.4% and 89.7%, respectively.

The multi-layer feed-forward ANN demonstrates satisfactory capability in this proposed scheme. The inputs include vehicle speed, the state of charge of both the SC and NMC-lithium battery, as well as the number of braking situations per drive cycle. The ANN algorithmic scheme generates regenerative braking force values for the front wheel as its outputs, utilizing a hidden layer consisting of five neurons. These neurons in the hidden layer employ sigmoid activation functions.

The optimization of the three-phase inverter switching scheme for the RBS was achieved using an ANN-equipped control mechanism. During regenerative braking, the ANN-equipped SC/NMC-lithium battery-RBS efficiently directed and stored braking energy in the SC [6].

In the initial scenario, the SC began with a state of charge of 85.2%, while the NMC-lithium battery started at a SOC of 87.7%. Since the SC voltage remained well below the safety threshold of 97%, the NMC-lithium battery regenerative braking did not engage. Consequently, only the SC was utilized to store energy from braking in this scenario. Considering the statuses of both the SC and the NMC-lithium battery in this scenario, the second braking case was used. In this case, the initial state of charge of the SC was set to 98.5%. Here, the capacitor's SOC exceeded the predefined safety threshold.

Table 5 provides a tabulation of the optimal simulation parameters for the HVA scheme. The HVA scheme was simulated using MATLAB under sinusoidal vibration conditions, with varying frequencies of 2.5, 3, 3.5, and 4 Hz and amplitudes of 3.5, 7, and 10.5 mm for the force–displacement loops. The sinusoidal vibration function can be expressed as follows, where x is the sinusoidal vibration, t is the period time or reciprocal of frequency, and π and ω are the amplitude and frequency of the sinusoidal vibration, respectively.

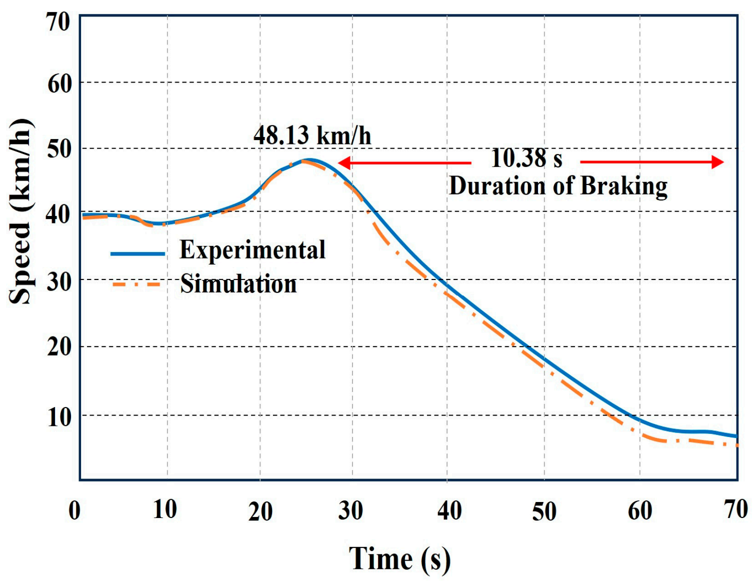

Figure 11. The simulations and experiments involving speed and the time required within a braking range of 10.38 s.

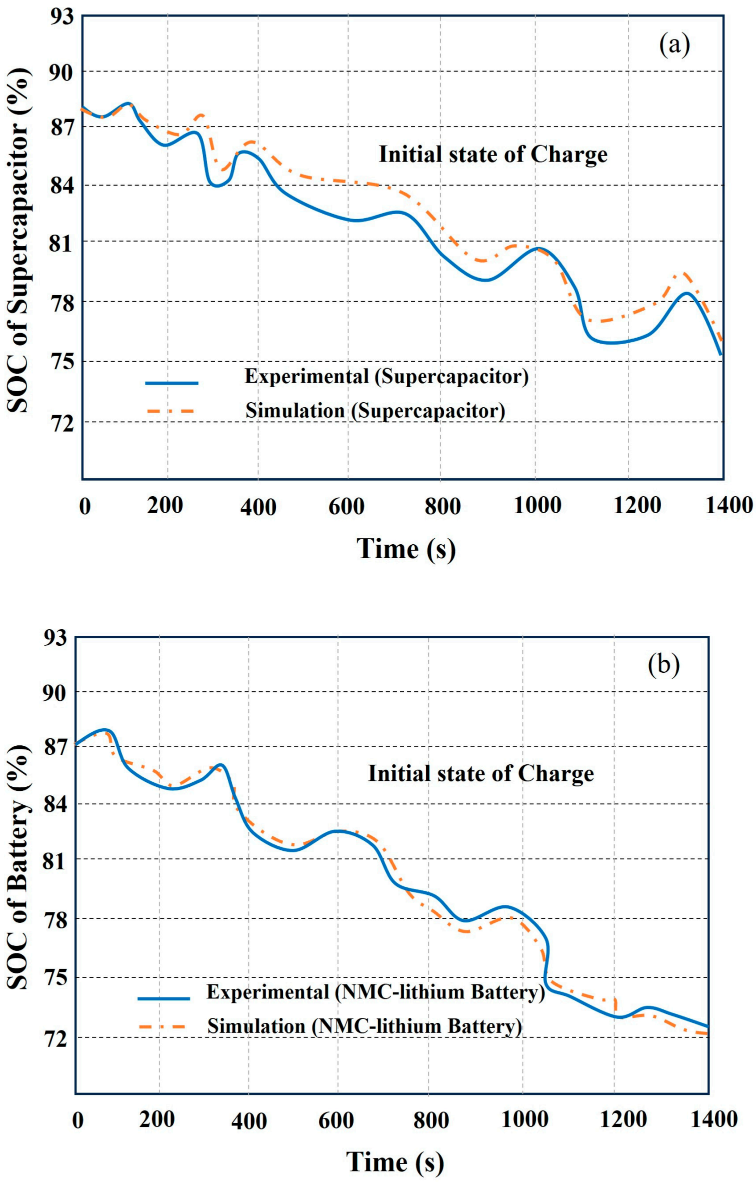

Figure 12. Represents the initial SOC of (**a**) the SC; (**b**) the NMC-lithium battery.

Table 5. The experimental optimal simulation parameters of the HVA.

Parameter	Symbol	Value
Pinion inertia	I_p	32.28 kg mm^2
Shaft inertia	I_s	3.25 kg mm^2
Bevel gear inertia	I_b	4.81 kg mm^2
Planetary gearbox inertia	I_{pg}	0.22 kg cm^2
Rotor inertia of generator	R_g	0.50 kg cm^2
Mass of external cylinder	m_c	3.40 kg
Mass of rack	m_r	0.20 kg
Rotary damping coefficient	k_e	0.05 V s/rad
Planetary gearbox ratio	i	1:30

In Figure 13a–c, the simulated force–displacement loops correspond to the proposed HVA scheme with amplitudes of 3.5, 7, and 10.5 mm, while considering frequencies of 2.5, 3, 3.5, and 4 Hz. The simulation results demonstrate that the HVA meets the criteria for traditional vibration absorbers, particularly in terms of damping and elasticity. The force–displacement loops exhibit an orientation that is non-horizontal and oblong-shaped, with the mass inertia being associated with the negative slope. Furthermore, achieving the ideal force–displacement loops is possible with the use of optimal simulation parameters.

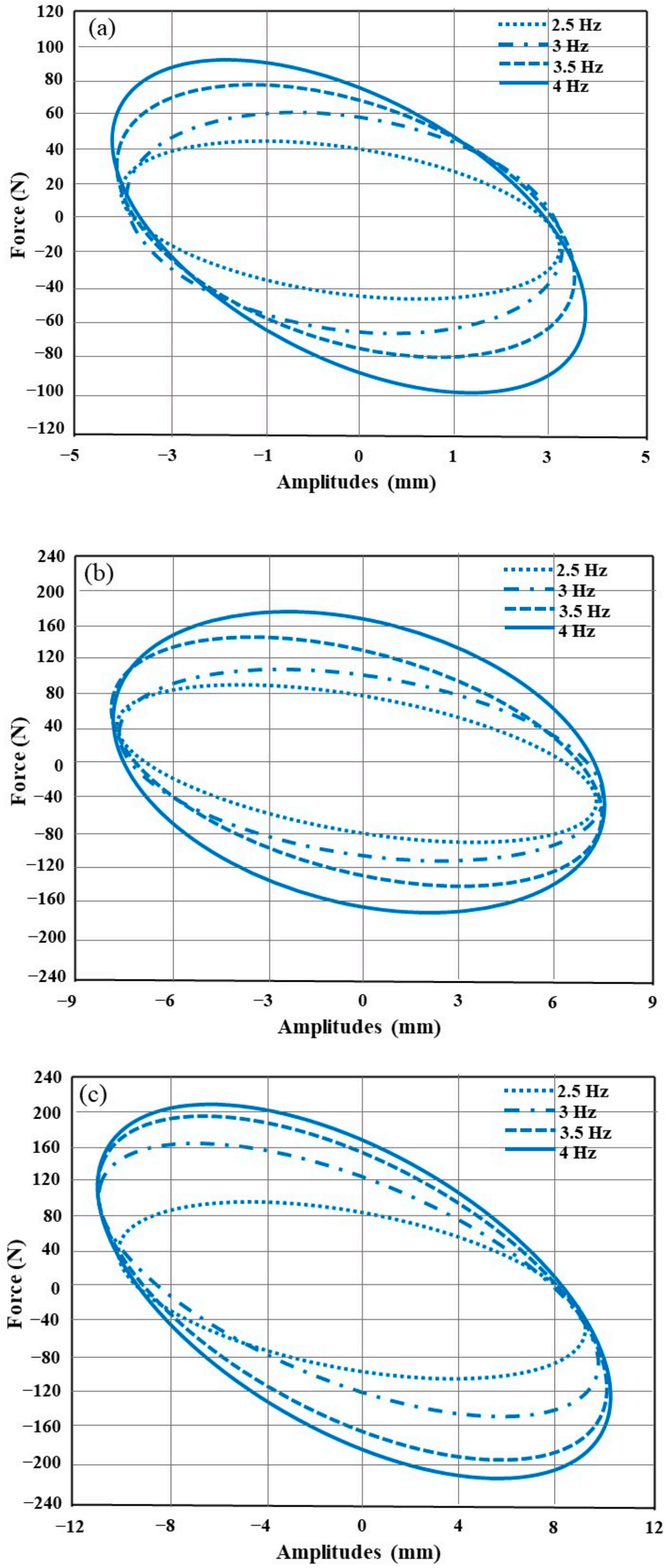

Figure 13. The simulated force–displacement loops for amplitudes of: (**a**) 3.5 mm; (**b**) 7 mm, and (**c**) 10.5 mm under the frequencies of 2.5, 3, 3.5, and 4 Hz.

The simulation results also indicated a positive correlation between the vibrational frequency and the slope of the force–displacement loop for amplitudes of 3.5, 7, and 10.5 mm. In simpler terms, an increase in the excitation frequency leads to an increase in the slope of the loops. The non-horizontal shape of the loops can be attributed to the masses of the outer cylinder (m_c) and the rack (m_r), as well as the inertia of various moving components, such as the pinions, shaft, bevel gears, planetary gearbox, and generator, as estimated by Equation (1). In contrast, when comparing, the simulated mechanical work input of the HVA (ΔW) (inner-loop area), increases as the amplitude (3.5, 7, 10.5 mm) increases while maintaining the same excitation frequency.

In Figure 14a–c, representations of the force–displacement loops for the HVA scheme are shown, where the amplitude is 9 **mm**. These loops were generated experimentally at frequencies of 2.5, 3, 3.5, and 4 Hz. Experiments have indicated a direct relationship between higher vibration frequencies and forces. This suggests that when more vibration is present, the system has the potential to store a greater amount of energy. The enclosed area within these loops corresponds to the mechanical work input (ΔW) associated with the HVA.

In Figure 15, there is a comparison of the driving distances and durations (driving cycles) of the MEV. In different configurations, the scenarios of three MEV systems are considered: only HVA, SCB-HESP-RBS, and SCB-HESP-RBS using HVA. Observations show that one propulsion cycle covers 10,000.95 **m** and takes 906.10 **s** to complete. The experiment found that MEV with only HVA could drive 164.25 km or 15 cycles, while MEV with SCB-HESP-RBS could drive 214.40 km or 19.5 cycles, and MEV with SCB-HESP-RBS using HVA could drive 247.34 km or 22.5 cycles. Figures 16 and 17 depict the instantaneous power and standalone voltage of the experimental external resistors, including the total experimental resistors, at a frequency of 4 Hz and amplitude of 10.5 mm. Tables 6 and 7 show the simulated and experimental output power (mechanical power), respectively, under varying frequencies and amplitudes. The results showed that the simulation and experimental results were in good agreement. Figure 18 shows the experimental total efficiency (β) of the HVA under variable frequencies (2.5, 3, 3.5, 4 Hz) and amplitudes (3.5, 7, 10.5 mm). With the given values of β_{RP}, β_B, β_{PG}, and β_G as 0.95, 0.98, 0.93, and 0.96, respectively, the mechanical efficiency (β_M) of the HVA is calculated to be 0.94. The electrical efficiency (β_E) of the HVA is 0.88. In addition, Table 8 shows an efficiency comparison of this result and other literature reviews. From the reported results, it was found that this research has energy harvesting efficiency comparable to that found in other literature reviews.

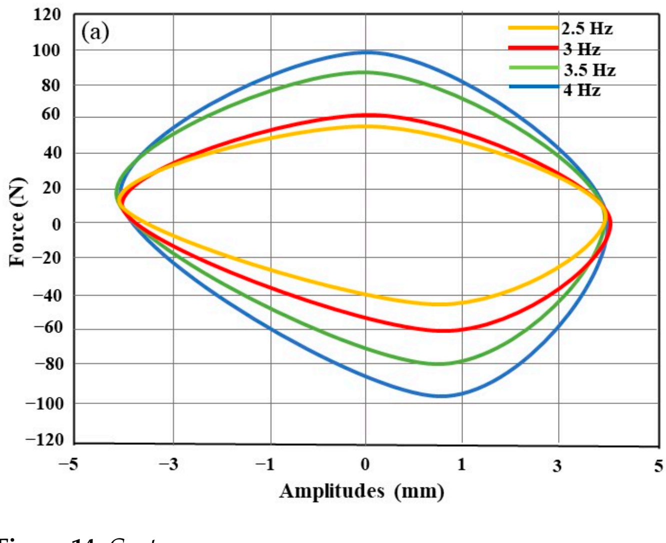

Figure 14. *Cont.*

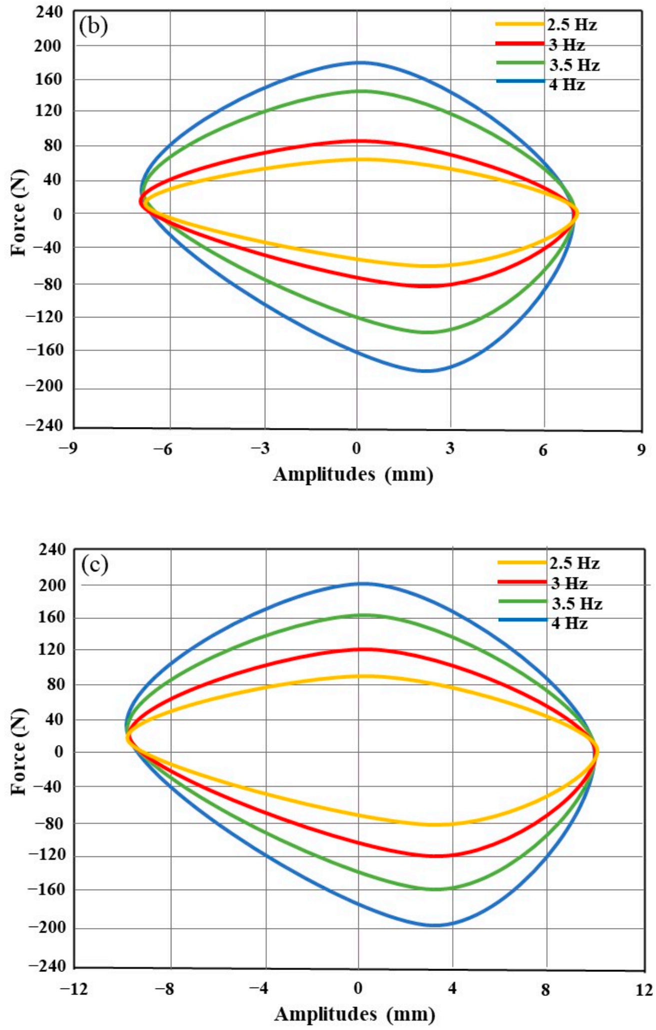

Figure 14. The force–displacement loops were obtained through experimental techniques at frequencies of 2.5, 3, 3.5, and 4 Hz given the amplitudes of (**a**) 3.5 mm; (**b**) 7 mm, (**c**) 10.5 mm.

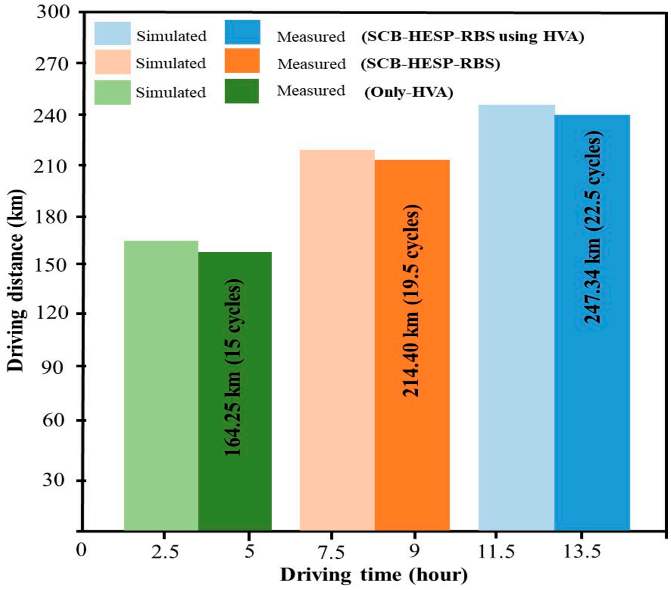

Figure 15. The driving ranges of the MEV under three different conditions: with only-HVA, SCB-HESP-RBS, and SCB-HESP-RBS using HVA.

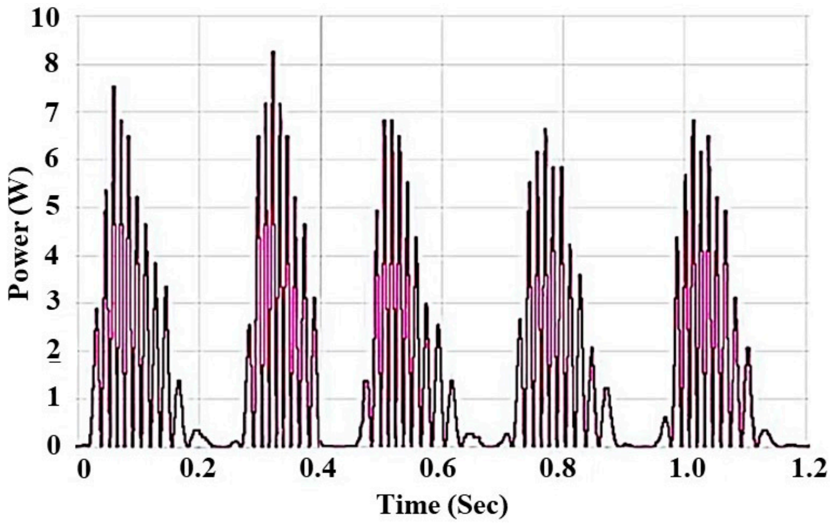

Figure 16. Instantaneous electrical power of the external resistor at 4 Hz and an amplitude of 10.5 mm.

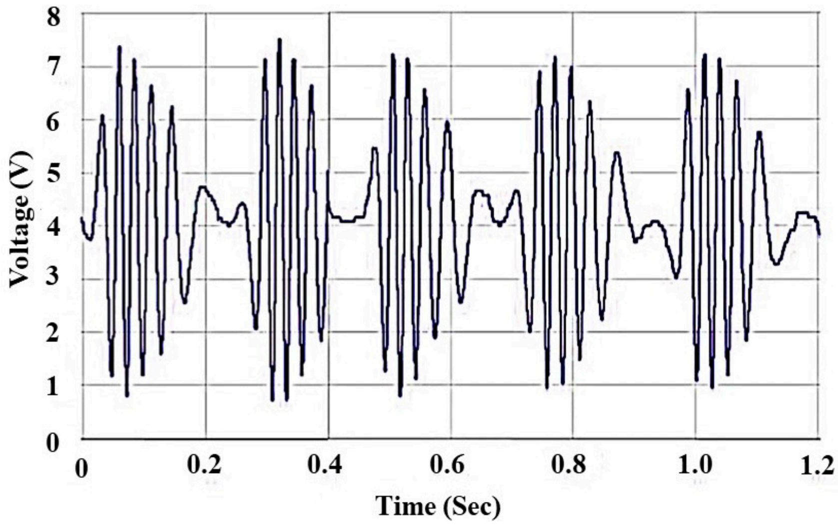

Figure 17. Voltage of the external resistor at a frequency of 4 Hz and an amplitude of 10.5 mm.

Table 6. Simulated electrical power of HVA under variable frequencies and amplitudes.

Amplitude \ Frequency	2.5 Hz	3 Hz	3.5 Hz	4 Hz
3.5 mm	1.105 W	1.302 W	1.795 W	2.401 W
7 mm	1.547 W	1.898 W	2.973 W	3.805 W
10.5 mm	1.976 W	2.894 W	4.035 W	8.401 W

Table 7. Experimental electrical power of HVA under variable frequencies and amplitudes.

Amplitude \ Frequency	2.5 Hz	3 Hz	3.5 Hz	4 Hz
3.5 mm	0.938 W	1.194 W	1.589 W	2.091 W
7 mm	1.382 W	1.598 W	2.712 W	3.672 W
10.5 mm	1.827 W	2.692 W	3.894 W	8.253 W

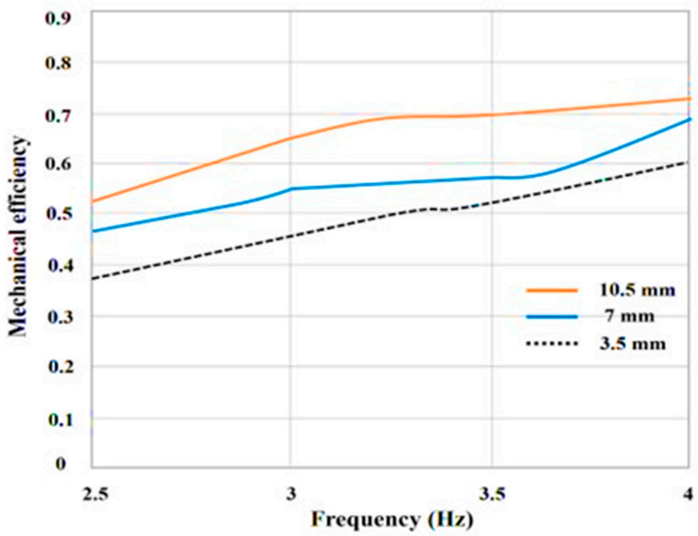

Figure 18. The total efficiency (β) of the HVA varies with both frequencies and amplitudes.

Table 8. Comparison of efficiency of energy harvesting according to other literature reviews.

Energy Harvesting Type	Efficiency	Ref.
SCB-HESP-RBS using HVA	50.58%	This work
SC/Battery using shock absorber	45%	[28]
SC/Battery using shock absorber	62%	[29]
SC/Battery using shock absorber	39.3%	[30]
SC/Battery using shock absorber	39.46%	[31]

7. Conclusions

This research proposed an up-scaling of the hybrid energy harvesting paradigm (HEHP) from the laboratory into a real vehicle for a MEV driven by PMSM at 30 kW. This system combines the unique characteristics of SC and batteries, also known as the hybrid energy storage paradigm (SCB-HESP), and integrates it with RBS and HVA, which can enhance the efficiency of electric vehicles. In the regenerative braking scenario, the ANN mechanism controls the RBS to adjust the switching waveform of the three-phase power inverter and transfers the braking energy to the energy storage device. As for the purpose, HVA-equipped in SC consists of three main parts: the suspension harvesting system, a conversion mechanism, and energy storage modules. When the vehicle moves along a rough road, the vibration of the harvesting energy is converted by generator module into electrical energy and transferred to storage in SC, which can help to extend the battery life and driving range. In an experiment comparing driving between three different systems, MEV only-HVA, SCB-HESP-RBS, and SC-HESP-RBS using HVA in an NEDC standard, given one drive cycle of 10.95 km, it was found that MEV with only HVA could drive 164.25 km (15 cycles), while MEV with SCB-HESP-RBS could drive 214.40 km (19.5 cycles), and MEV with SCB-HESP-RBS using HVA could drive 247.34 km (22.5 cycles). The efficiency of energy harvesting of MEV based on SCB-HESP-RBS using HVA suspended energy harvesting was enhanced up to 50.58% and 15.36% in comparison with MEV with only-HVA and SCB-HESP-RBS, respectively.

Author Contributions: Conceptualization, P.T.; methodology, P.T. and P.S.; software, P.T.; validation, P.T. and P.S.; formal analysis, P.T. and P.S.; investigation, P.T.; resources, P.T. and P.S.; data curation, P.T. and P.S.; writing—original draft preparation, P.T. and P.S.; writing—review and editing, P.T. and P.S.; visualization, P.T. and P.S.; supervision, P.T.; project administration, P.T. and P.S.; funding acquisition, P.T. and P.S. All authors have read and agreed to the published version of the manuscript.

Funding: This research received no external funding.

Data Availability Statement: The original contributions presented in the study are included in the article, further inquiries can be directed to the corresponding author.

Conflicts of Interest: The authors declare no conflict of interest.

Abbreviations

The abbreviations utilized in this paper are outlined as follows:

Abbreviation	**Full Name**
HEHP	Hybrid energy harvesting paradigm
HESP	Hybrid energy storage paradigm
SC	Supercapacitor
NMC	Nickel–magnesium–cobalt
SC/NMC	Supercapacitor and nickel–magnesium–cobalt
SCB-HESP	Supercapacitor and battery hybrid energy storage paradigm
RBS	Regenerative braking system
SCB-HESP-RBS	Supercapacitor and battery hybrid energy storage paradigm equipped regenerative braking system
MEV	Gross weight 2 tons electric vehicles
PMSM	Permanent magnet synchronous motors
BLDC	Brushless direct current motor
ANN	Advanced artificial neural network
SOC	States of charge
IGBTs	Insulated gate bipolar transistors
PID	Proportional Integral Derivative

References

1. Aminzadegan, S.; Shahriari, M.; Mehranfar, F.; Abramovi, B. Factors affecting the emission of pollutants in different types of transportation: A literature review. *Energy Rep.* **2022**, *8*, 2508–2529. [CrossRef]
2. Janos, L.B.; Remzi, C.S.; Detlef, S.; Ralf, P. How to reduce the greenhouse gas emissions and air pollution caused by light and heavy-duty vehicles with battery-electric, fuel cell-electric and catenary trucks. *Environ. Int.* **2021**, *152*, 106474. [CrossRef] [PubMed]
3. Janos, L.B.; Remzi, C.S.; Ralf, P.; Stolten, D. The impact of diesel vehicles on NOx and PM10 emissions from road transport in urban morphological zones: A case study in North Rhine-Westphalia, Germany. *Sci. Total Environ.* **2020**, *727*, 138583. [CrossRef] [PubMed]
4. Ercan, T.; Nuri, C.O.; Keya, N.; Tatari, O.; Eluru, N.; Kucukvar, M. Autonomous electric vehicles can reduce carbon emissions and air pollution in cities. *Transp. Res. D Transp. Environ.* **2022**, *112*, 103472. [CrossRef]
5. Shahzad, M.; Shafiq, M.T.; Douglas, D.; Kassem, M. Digital Twins in Built Environments: An Investigation of the Characteristics, Applications, and Challenges. *Buildings* **2022**, *12*, 120. [CrossRef]
6. Kiddee, K. Hybrid Energy Harvesting System Based on Regenerative Braking System and Suspension Energy Harvesting for Middle Electric Vehicle. *J. Eng. Technol.* **2020**, *8*, 29–38.
7. Sharma, R.; Kumar, H.; Gaman, K.; Sharma, S.; Aneja, R.; Sharma, A.K.; Kumar, R.; Kumar, P. Progress and challenges in electrochemical energy storage devices: Fabrication, electrode material, and economic aspects. *J. Chem. Eng.* **2023**, *468*, 143706. [CrossRef]
8. Asensio, E.M.; Magallán, G.A.; Angelo De, C.H.; Federico, M.S. Energy Management on Battery/Ultracapacitor Hybrid Energy Storage System based on Adjustable Bandwidth Filter and Sliding-mode Control. *J. Energy Storage* **2020**, *30*, 101569. [CrossRef]
9. Abdelkareem, M.A.A.; Xu, L.; Ali, M.K.A.; Elagouz, A.; Mi, J.; Guo, S.; Liu, Y.; Zuo, L. Vibration energy harvesting in automotive suspension system: A detailed review. *Appl. Energy* **2018**, *229*, 672–699. [CrossRef]
10. Santucci, A.; Sorniotti, A.; Lekakou, C. Power split strategies for hybrid energy storage systems for vehicular applications. *J. Power Sources.* **2014**, *258*, 395–407. [CrossRef]
11. Shen, J.; Khaligh, A. A supervisory energy management control strategy in a battery/ultracapacitor hybrid energy storage system. *IEEE Trans. Transp. Electrif.* **2015**, *1*, 223–231. [CrossRef]
12. Qiu, C.; Wang, G.; Meng, M.; Shen, Y. A novel control strategy of regenerative braking system for electric vehicles under safety critical driving situations. *Energy* **2018**, *149*, 329–340. [CrossRef]
13. Kuperman, A.; Aharon, I.; Malki, S.; Kara, A. Design of a semiactive battery-ultracapacitor hybrid energy source. *IEEE Trans. Power Electron.* **2013**, *28*, 806–815. [CrossRef]
14. Myeong, H.H.; Lee, G.S.; Kim, E.; Kim, H.W.; Yoon, S.; Talluri, T.; Cha, H.R. Regenerative Braking Control Strategy Based on AI Algorithm to Improve Driving Comfort of Autonomous Vehicles. *Appl. Sci.* **2023**, *13*, 946. [CrossRef]

15. Wang, Z.; Zhang, T.; Zhang, Z.; Yuan, Y.; Liu, Y. A high-efficiency regenerative shock absorber considering twin ball screws transmissions for application in range-extended electric vehicles. *Energy Built Environ.* **2020**, *1*, 36–49. [CrossRef]
16. Wai, C.K.; Rong, Y.Y. Electric Vehicle Energy Harvesting System Regenerative Shock Absorber for Electric Vehicle. In Proceedings of the 2013 IEEE Conference on Sustainable Utilization and Development in Engineering and Technology (CSUDET), Selangor, Malaysia, 30 May 2013; pp. 7–10. [CrossRef]
17. Yang, X.F.; Zhao, W.T.; Liu, Y.L.; Chen, L.; Meng, X.P. Design and experimental study of the energy-regenerative circuit of a hybrid vehicle suspension. *Sci. Prog.* **2020**, *103*, 0036850419874999. [CrossRef] [PubMed]
18. Kim, J.H.; Shin, Y.J.; Chun, Y.D.; Kim, J.H. Design of 100W regenerative vehicle suspension to harvest energy from road surfaces. *Int. J. Precis. Eng. Manuf.* **2018**, *19*, 1089–1096. [CrossRef]
19. Dahat, N.; Maskar, P.; Yadav, A. Design and development of regenerative shock absorber. *Mater. Today Proc.* **2023**, *82*, 363–368. [CrossRef]
20. Arroyo, E.; Badel, A.; Formosa, F. Energy harvesting from ambient vibrations: Electromagnetic device and synchronous extraction circuit. *J. Intell. Mater. Syst. Struct.* **2013**, *24*, 2023–2035. [CrossRef]
21. Lei, Z.; Qin, D.; Hou, L.; Peng, J.; Liu, Y.; Chen, Z. An adaptive equivalent consumption minimization strategy for plug-in hybrid electric vehicles based on traffic information. *Energy* **2020**, *190*, 116409. [CrossRef]
22. Xie, S.; Hu, X.; Xin, Z.; Li, L. Time-efficient stochastic model predictive energy management for a plug-in hybrid electric bus with an adaptive reference state-of-charge advisory. *IEEE Trans. Veh. Technol.* **2018**, *67*, 5671–5682. [CrossRef]
23. Zhang, Y.; Chen, Z.; Li, G.; Liu, Y.; Huang, Y. A Novel Model Predictive Control Based Co-Optimization Strategy for Velocity Planning and Energy Management of Intelligent PHEVs. *IEEE Trans. Veh. Technol.* **2022**, *71*, 12667–12681. [CrossRef]
24. Naseri, F.; Barbu, C.; Sarikurt, T. Optimal sizing of hybrid high-energy/high-power battery energy storage systems to improve battery cycle life and charging power in electric vehicle applications. *J. Energy Storage* **2022**, *55*, 105768. [CrossRef]
25. Naseri, F.; Farjah, E.; Ghanbari, T. An efficient regenerative braking system based on battery/supercapacitor for electric, hybrid, and plug-in hybrid electric vehicles with BLDC motor. *IEEE Trans. Veh. Technol.* **2016**, *66*, 3724–3738. [CrossRef]
26. Levesque, W.; Bégin-Drolet, A.; Lépine, J. Effects of Pavement Characteristics on Rolling Resistance of Heavy Vehicles: A Literature Review. *J. TRR.* **2023**, *6*, 296–309. [CrossRef]
27. Kiddee, K.; Sukcharoensup, T. In Efficiency Analysis of Suspension Energy Harvesting besed on Supercapacitor for Electric Vehicles. In Proceedings of the 2020 8th International Electrical Engineering Congress (iEECON), Chiang Mai, Thailand, 4–6 March 2020; pp. 1–4. [CrossRef]
28. Puliti, M.; Galluzzi, R.; Tessari, F.; Amati, N.; Tonoli, A. Energy efficient design of regenerative shock absorbers for automotive suspensions: A multi-objective optimization framework. *Appl. Energy* **2024**, *358*, 122542. [CrossRef]
29. Salman, W.; Zhang, X.; Li, H.; Wu, X.; Li, N.; Azam, A.; Zhang, Z. A novel energy regenerative shock absorber for in-wheel motors in electric vehicles. *Mech. Syst. Signal Process.* **2022**, *181*, 109488. [CrossRef]
30. Abdelrahman, M.; Liu, G.; Fan, C.; Zhang, Z.; Ali, A.; Li, H.; Azam, A.; Cao, H.; Mohamed, A.A. Energy regenerative shock absorber based on a slotted link conversion mechanism for application in the electrical bus to power the low wattages devices. *Appl. Energy* **2023**, *347*, 121409. [CrossRef]
31. Li, H.; Zheng, P.; Zhang, T.; Zou, Y.; Pan, Y.; Zhang, Z.; Azam, A. A high-efficiency energy regenerative shock absorber for powering auxiliary devices of new energy driverless buses. *Appl. Energy* **2021**, *295*, 117020. [CrossRef]